Chaos
An Interdisciplinary Journal of Nonlinear Science

RESEARCH ARTICLE | FEBRUARY 03 2026

Accurate and robust real-time prediction of September Arctic sea ice

Special Collection: Responsible Forecasting in Climatology and Environmental Sciences

Dmitri Kondrashov ; Ivan Sudakow ; Valerie Livina ; Qingping Yang

Chaos 36, 023110 (2026)
https://doi.org/10.1063/5.0295634

Accurate and robust real-time prediction of September Arctic sea ice

Cite as: Chaos 36, 023110 (2026); doi: 10.1063/5.0295634
Submitted: 9 August 2025 · Accepted: 7 December 2025 ·
Published Online: 3 February 2026

Dmitri Kondrashov,[1] Ivan Sudakow,[2,3,a)] Valerie Livina,[4] and Qingping Yang[5]

AFFILIATIONS

[1]Department of Atmospheric and Oceanic Sciences, University of California, Los Angeles, California 90095, USA
[2]School of Mathematics and Statistics, The Open University, Milton Keynes MK7 6AA, United Kingdom
[3]The Carl Sagan Center for Research, The SETI Institute, Mountain View, California 94043, USA
[4]Data Science & AI Department, National Physical Laboratory, Teddington, United Kingdom
[5]College of Engineering, Design and Physical Sciences, Brunel University of London, Uxbridge UB8 3PH, United Kingdom

Note: This paper is part of the Special Topic on Responsible Forecasting in Climatology and Environmental Sciences.
[a)]**Author to whom correspondence should be addressed:** ivan.sudakow@open.ac.uk

ABSTRACT

We describe the real-time forecasting of September 2024 Arctic sea ice extent using a theory-guided machine learning method based on data-adaptive harmonic decomposition and frequency-based nonlinear stochastic modeling, as part of the Sea Ice Outlook. Compared to standard statistical and machine learning models, this method adeptly accounts for non-linear behavior, effectively incorporates memory effects, and handles a wide range of time scale variations, from synoptic (stochastic-like) weather effects to low-frequency (red-noise like) variability, significantly enhancing the accuracy and reliability of sea ice prediction.

This paper presents real-time seasonal forecasting of Arctic sea ice cover in September using advanced machine learning approach inspired by concepts from statistical mechanics and data-driven nonlinear stochastic climate modeling.

I. INTRODUCTION

Arctic sea ice is a critical component of the Earth's climate system, reflecting sunlight to cool the planet and influencing ocean circulation, weather patterns, and polar ecosystems. Its rapid decline—driven by long-term climate change—has far-reaching impacts, including increased maritime activity, ecosystem changes, and accelerated warming due to the ice-albedo feedback loop. The Sea Ice Outlook (SIO) (Hamilton and Stroeve, 2016; Blanchard-Wrigglesworth *et al.*, 2023) is an international effort to provide a community-wide summary of predictions for the Arctic sea ice in September, that is typically a minimum of sea ice cover in a calendar year. It has been managed by the Sea Ice Prediction Network (SIPN), under the Arctic Research Consortium of the United States (ARCUS), with support from organizations like the National Science Foundation (NSF), the National Oceanic and Atmospheric Administration (NOAA), and the National Snow and Ice Data Center (NSIDC). The SIO has been running since 2008 and aims to synthesize forecasts from scientists, stakeholders, and citizen scientists to improve seasonal sea ice predictions, using both physics-based and statistical models. The SIO does not issue definitive predictions but compiles and summarizes available data, observations, and model outputs to provide the best possible information on Arctic sea ice conditions. It focuses on both pan-Arctic and regional sea ice extent (SIE), offering insights into seasonal trends and variability. The SIO's collaborative approach enhances scientific understanding of Arctic climate changes and supports decision-making in the Arctic.

SIO monthly reports are released during the summer (June, July, August, and lately September) based on data from May through August. The SIO emphasizes the September sea ice minimum because it is a critical indicator of Arctic sea ice health, reflecting long-term trends and interannual variability. Arctic sea ice extent has declined by about 40% since 1979, with notable lows in 2007 and 2012. Seasonal sea ice prediction is challenging due to the variable nature of weather and ocean behavior. While short-term (up to

two weeks) and long-term (decadal) forecasts can be reliable, 1–3 month predictions are less accurate. The SIO aims to identify the most effective models and methods to improve forecasting skill, particularly for regional predictions, which are critical for stakeholders like shipping industries, fisheries, and Arctic communities.

Real-time forecasts of 2016–2024 September SIE by statistical model utilizing Data-adaptive Harmonic Decomposition (DAHD) modeling (Sec. III), turned out to be fairly accurate and very competitive among statistical and dynamical models in the SIO submissions. The average of summertime DAHD-based predictions (June, July, and August) was within 0.3 million km^2 of the observed September pan-Arctic SIE for seven years in a row (except 2020 that was challenging for all the models), given Pan-Arctic SIE area of ≈5.0 million km^2, and typical multi-model SIO spread of lower–upper quartiles ≈0.6 million km^2 per SIO post-season reports (Meier *et al.*, 2021; Bhatt *et al.*, 2019, 2020, 2022, 2023). Also, DAHD-based predictions for the Alaska region solicited by SIO have been similarly accurate (available in post-season reports). In this paper, we focus on and detail DAHD predictions made in 2024.

II. DATA

We have used average daily sea ice extent from 1978 to present, using 5-day trailing averages, in square kilometers, by region of the Arctic Ocean. Data are from the NSIDC Sea Ice Index Fetterer *et al.* (2017) from the Defense Meteorological Satellite Program (DMSP) series of passive microwave remote sensing instruments. The Sea Ice Index is based on the Near-Real-Time DMSP SSM/I-SSMIS Daily Polar Gridded Sea Ice Concentrations and the NASA-produced Sea Ice Concentrations from Nimbus-7 SMMR and DMSP SSM/I Passive Microwave Data. The original daily Arctic SIE data were averaged into a weekly resolution of 52 weeks in each calendar year and combined over several large Arctic regions, see Fig. 1. Figure 2 shows September sea ice extent (SIE) evolution by region summing to pan-Arctic SIE, namely, Center, Beaufort and Chukchi seas, Canadian Archipelago, Barents and Kara seas, Laptev and East Siberian seas, Baffin bay and Greenland sea, and finally Other (Bering sea, Hudson bay, Sea of Okhotsk, and St. Lawrence) where there is typically little or no ice left at the peak of the melt season in September. The Pan-Arctic SIE experiences a long-term downward trend with a rapid decline from 1990 through 2000s, and driven primarily by changes in Beaufort/Chukchi and Laptev/East Siberian regions. However, in recent years, the rate of reduction in the summertime extent has slowed considerably as compared to the early part of the 21st century, and September SIE has fluctuated with a large inter-annual variability including absolute minimum in 2012 but exhibits no long-term trend (Stern, 2025). For this reason, we focus on 2006–2024 time span.

Figure 3 illustrates the weekly evolution of regional and pan-Arctic SIE from 2006 to 2024 throughout the summer for each year. Figure 4 depicts the corresponding anomalies after subtracting the seasonal cycle, showing varied evolution across years. Regional Arctic sea ice in 2024 retreated seasonally until July, when melting accelerated due to significant ice loss in the Laptev and East Siberian Seas caused by warmer conditions. In August, the Beaufort and Chukchi Seas, which had melted slowly earlier in the season, became the primary areas of ice retreat. By early September, the rate of ice loss slowed, except in the Canadian Archipelago, where it continued to decline rapidly through September.

III. DATA-ADAPTIVE HARMONIC DECOMPOSITION (DAHD)

Data-adaptive harmonic decomposition (DAHD) (Chekroun and Kondrashov, 2017) integrates *statistical identification* of spatiotemporal modes with *their nonlinear stochastic modeling*. DAHD is realized numerically by the eigendecomposition of grand-block matrix constructed from space-pairwise, time-lagged cross correlations within specified time-embedding window M (in sampling units) or by a more computationally efficient and accurate implementation (Zerenner *et al.*, 2021) via frequency-ranked Hermitian cross-spectral density matrix formed by Fourier transforms of cross correlations (Kondrashov *et al.*, 2020), described below.

We consider a multivariate time series $\boldsymbol{X}(n) = (X_1(n), \ldots, X_d(n))$ formed with d spatial channels and $n = 1, \ldots, N$ time points (sampled evenly) and with zero mean. Space-pairwise, time-lagged cross-correlation coefficients $\rho^{(p,q)}(m)$ are estimated for all pairs of channels p and q and time lag m up to a maximum $M-1$,

$$\rho^{(p,q)}(m) = \begin{cases} \dfrac{1}{N-m}\sum_{n=1}^{N-m} X_p(n+m)X_q(n), & 0 \le m \le M-1, \\ \rho^{(q,p)}(-m), & m < 0. \end{cases} \tag{1}$$

Here, M is the embedding window and its size should be larger than typical decorrelation times in the data; it is the slowest temporal scale captured by DAHD. To reduce the biases of cross-correlation estimates, common lag windowing can be applied.

We can, thus, define cross-spectral density matrix $\boldsymbol{S}(f)$,

$$\boldsymbol{S}(f) = e^{-i\phi/2}\mathfrak{S}(f), \tag{2}$$

where $\mathfrak{S}_{p,q}(f) = \widehat{\rho^{p,q}}(f)$ for $1 \le p, q \le d$, $\widehat{\rho^{p,q}}(f)$ is the Fourier transform at the frequency f of the cross-correlation sequence $\rho^{p,q}(m)$,

$$\widehat{\rho^{p,q}}(f) = \sum_{m=-M+1}^{M-1} \rho^{p,q}(m)e^{-2\pi i f m}, \tag{3}$$

frequency f is equally spaced in the Nyquist interval [0 0.5] with M values,

$$f = \frac{(\ell-1)}{M'-1}, \quad \ell = 1, \ldots, M;\ M' = 2M-1, \tag{4}$$

and frequency-dependent phase-shift factor $e^{-i\phi/2}$ in Eq. (2) accounts for discrete case estimation with $\phi = \frac{2\pi(l-1)}{M'}$, $1 \le l \le M$. It is easy to show that Fourier transforms of $\rho^{q,p}(m)$ and $\rho^{p,q}(m)$ sequences are then related as

$$\widehat{\rho^{p,q}}(f) = e^{i\phi}\overline{\widehat{\rho^{q,p}}}(f), \tag{5}$$

where $\overline{\widehat{\rho^{q,p}}}$ is a complex conjugate. In numerical implementation practice matrix $\boldsymbol{S}$ is Hermitian, i.e., $\boldsymbol{S} = \boldsymbol{S}^* = \overline{\boldsymbol{S}^T}$ and it is interpreted as a correlogram estimate of multidimensional cross-spectral density $E\{\widehat{\boldsymbol{X}}(f)\widehat{\boldsymbol{X}}(f)^*\}$, where an expectation operator E is an ensemble average over different realizations of multidimensional random process $\boldsymbol{X}$. For univariate case, in particular (i.e., $p = q = 1$),

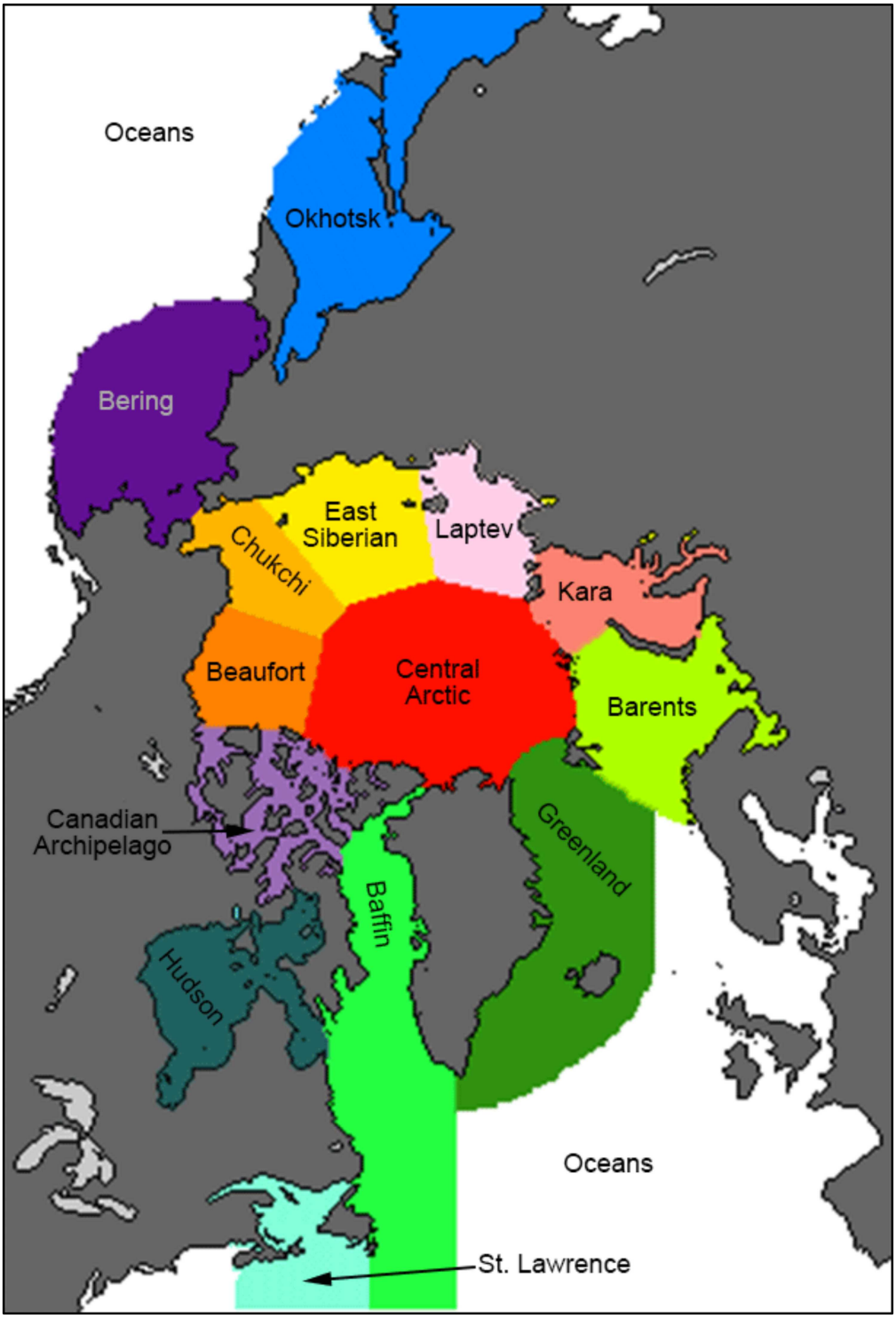

FIG. 1. Map of Arctic regions (from NSIDC SIE documentation).

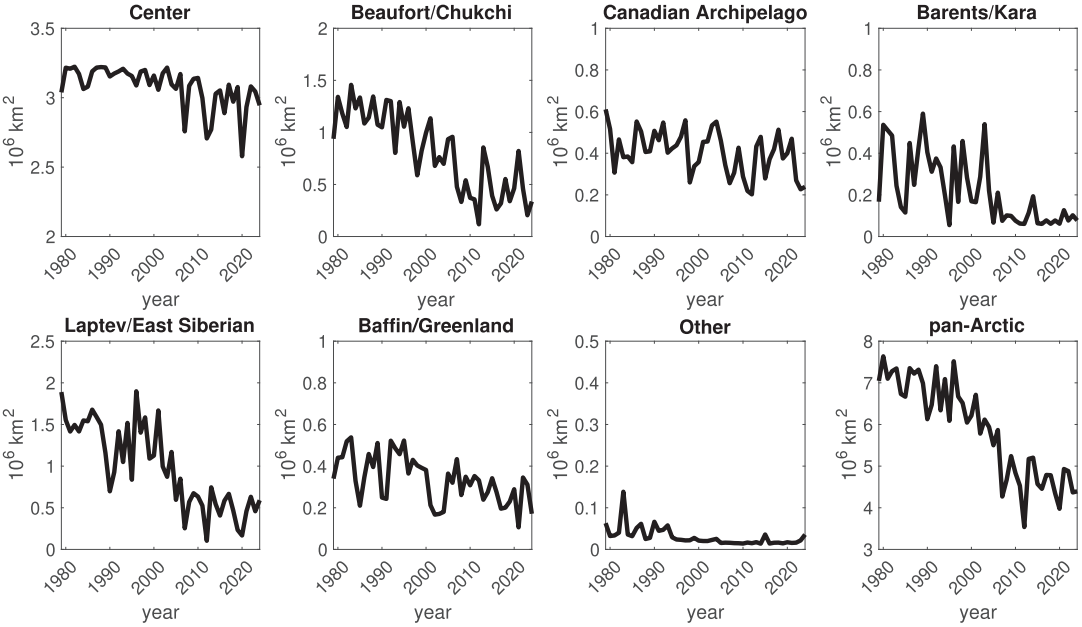

FIG. 2. Evolution of regional and pan-Arctic September SIE.

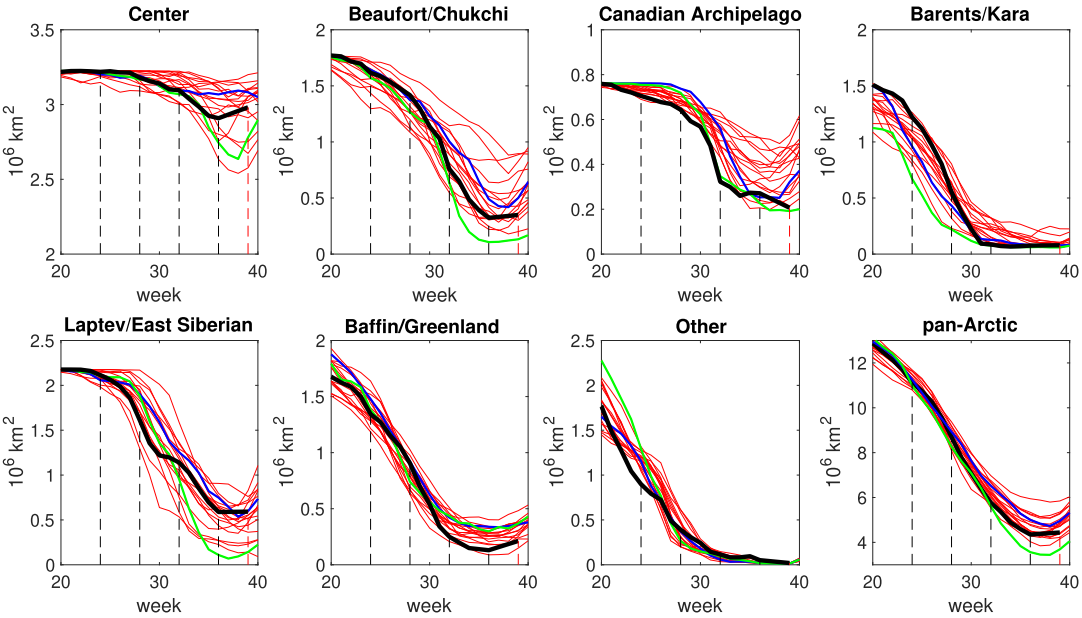

FIG. 3. Evolution of 2006–2024 regional and pan-Arctic SIE throughout the summer (red), 2024 (black), 2023 (blue), and 2012 (green). Vertical lines correspond to SIO predictions issued in June, July, August, and September (dashed black) through the end of September (dashed red).

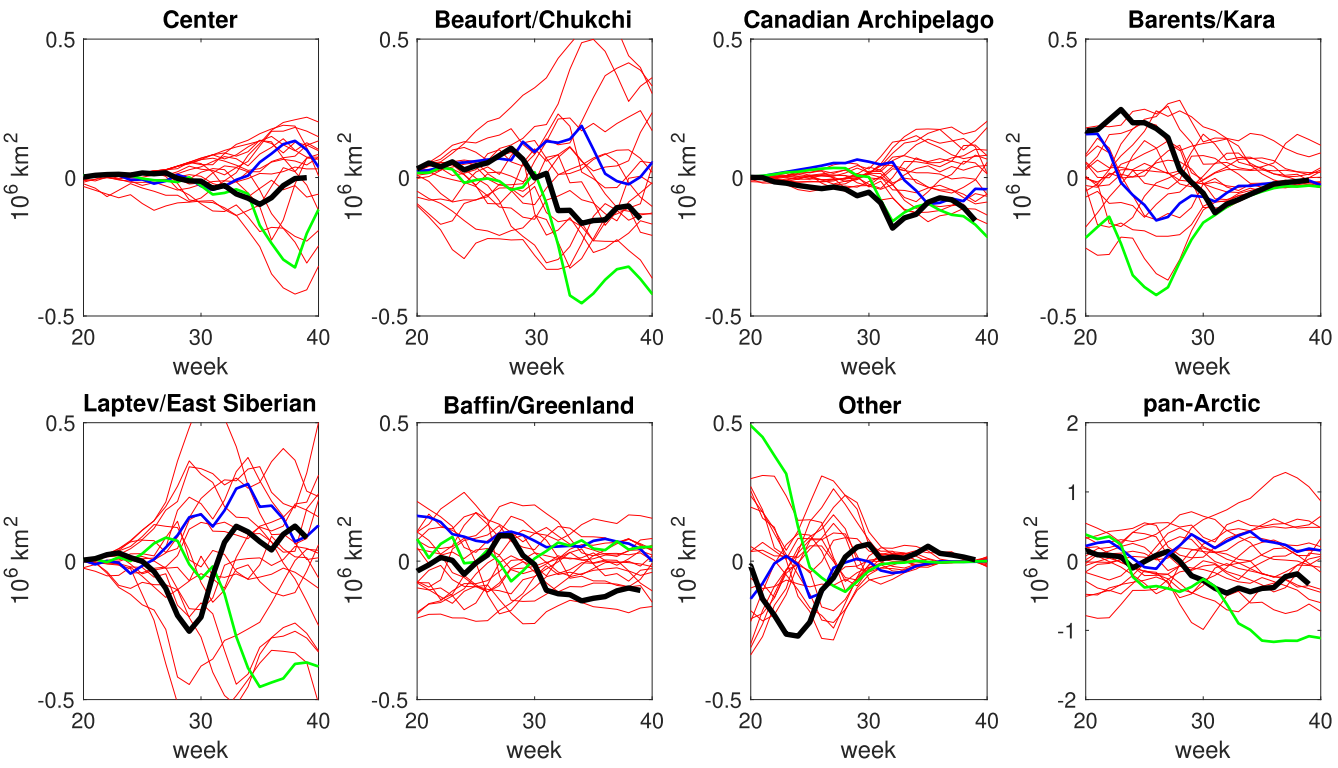

FIG. 4. Evolution of 2006–2024 regional and pan-Arctic SIE anomalies in summer (red), 2024 (black), 2023 (blue), and 2012 (green).

$S(f) = |\widehat{\rho(f)}|$ represents a well established correlogram method based on Wiener-Khinchin theorem, which states that the power spectral density is equal to the Fourier transform of its autocorrelation function (Percival and Walden, 1993). Furthermore, since $\boldsymbol{S}(f)$ is a Hermitian matrix, its eigendecomposition,

$$\boldsymbol{S}(f) = \boldsymbol{U}\boldsymbol{\Lambda}\boldsymbol{U}^*, \tag{6}$$

yields a set of d real positive eigenvalues $\Lambda = \mathrm{diag}(\lambda_1, \ldots, \lambda_d)$. Associated d eigenvectors $\boldsymbol{U}$ form an orthonormal set at each frequency f in the Nyquist interval [see Eq. (4)] and are associated with the Fourier transform of the time-domain data-adaptive harmonic modes (DAHMs) $\boldsymbol{W}_k$: $\boldsymbol{U_k}(f) = \widehat{\boldsymbol{W_k}}(f)$.

For the purpose of reconstruction in time domain for each λ_k, pairs $(\widehat{\boldsymbol{W_k^+}}(f) = \boldsymbol{U_k}(f), \widehat{\boldsymbol{W_k^-}}(f) = e^{i\pi/2}\boldsymbol{U_k}(f))$ are formed. In turn, $\boldsymbol{W_k^+}(f)$ and $\boldsymbol{W_k^-}(f)$ are obtained by inverse Fourier transform to yield space-time patterns at a single temporal frequency f and shifted by a quarter of a period (i.e., *sine* and *cosine* components) and, thus, provide an orthonormal basis set of modes $\mathbf{W}$ in time domain across all frequencies, i.e., $\mathbf{W}^T\mathbf{W} = \mathbf{I}$.

The combined set of $\mathbf{W}_j = \left(\mathbf{E}_1^j, \ldots, \mathbf{E}_d^j\right)$ represents global space-time patterns at specific temporal frequencies and without mixing of temporal scales. In particular, $\mathbf{E}_k^j$ is M'-long time series that corresponds to harmonic oscillation with a frequency f,

$$\mathbf{E}_k^j(s) = B_k^j \cos\left(2\pi f s + \theta_k^j\right), \quad 1 \le s \le M';\ 1 \le k \le d, \tag{7}$$

where the amplitudes B_k^j and phases θ_k^j are data-adaptive.

The original dataset $\mathbf{X}$ can be projected onto the orthogonal set formed by the $\mathbf{W}_j$s, in order to obtain the following *data-adaptive harmonic coefficients (DAHCs)*:

$$\xi_j(t) = \sum_{s=1}^{M'} \sum_{k=1}^{d} X_k(t+s-1)\mathbf{E}_k^j(s), \tag{8}$$

where t varies from 1 to

$$N' = N - M' + 1. \tag{9}$$

In particular, projection of original spatiotemporal field onto a pair of DAHMs $(\boldsymbol{W_k^+}(f), \boldsymbol{W_k^-}(f))$ associated with a given λ_k yields a set of narrow-band time series pairs $(p_k(t), q_k(t))$ (roughly in phase quadrature). Note that without using time-embedding, i.e., when $M = 1$, DAHD is reduced to eigendecomposition of spatial covariance matrix and, thus, it yields the same modes as Principal Component Analysis. The Hermitian DAHD formulation [Eq. (6)] closely resembles the spectral proper orthogonal decomposition (SPOD)/spectral empirical orthogonal functions (SEOF) approach (Towne, 2018; Schmidt *et al.*, 2019), with the key difference is that

the latter considers Welch's overlapped averaging periodogram estimate of cross-spectral density matrix and yields modes that can be thought as optimally averaged Dynamical Mode Decomposition (DMD) modes, accounting for the statistical variability, while the former is based on correlogram estimate [Eq. (2)]. By analogy with SPOD/SEOF modes, DAHD modes can be interpreted then as optimal response modes of the forced linear system if the forcing is white in space and time (Towne, 2018; Schmidt *et al.*, 2019).

Furthermore, DAHD eigenvectors and eigenvalues approximate Koopman operator eigenfrequencies together with the associated energy from given time series (Zhen *et al.*, 2022), respectively, which characterizes evolution of complex and nonlinear dynamical system in terms of an infinite-dimensional linear operator acting on partial observable from this system (Brunton *et al.*, 2022).

The original d-dimensional spatiotemporal field $\mathbf{X}$ with its multiple time scales is decomposed into DAHCs and then modeled by a network of frequency-based nonlinear stochastic Stuart–Landau (SL) oscillators (Kondrashov *et al.*, 2018),

$$\begin{aligned} dp_k/dt &= \beta_k(f)p_k - \alpha_k(f)q_k - \sigma_k(f)p_k\left(p_k^2+q_k^2\right) \\ &\quad + \sum_{i\neq k}^{d} a_{ik}(f)p_i + \sum_{i\neq k}^{d} b_{ik}(f)q_i + \epsilon_k^p, \\ dq_k/dt &= \alpha_k(f)p_k + \beta_k(f)q_k - \sigma_k(f)q_k\left(p_k^2+q_k^2\right) \\ &\quad + \sum_{i\neq k}^{d} c_{ik}(f)p_i + \sum_{i\neq k}^{d} d_{ik}(f)q_i + \epsilon_k^q, \end{aligned} \tag{10}$$

where $1 \le k \le d$, model parameters are estimated by pairwise multiple linear regression with linear constraints on $\alpha_k(f)$ and $\beta_k(f)$ to ensure antisymmetry for the linear coupling within the given DAHC pair (p_k, q_k). Among the possible constraints on $\sigma_k(f)$ in nonlinear term, applying the opposite sign improved numerical stability and prediction accuracy. This setup effectively models opposing feedback mechanisms, where one component (e.g., p_k) is stabilized nonlinearly while the other (e.g, q_k) is amplified.

The regression residuals $\left(\epsilon_k^p, \epsilon_k^q\right)$ from the main model level have their time evolution modeled by an additional layer, which depends linearly on $\left(\epsilon_k^p, \epsilon_k^q\right)$ and (p_k, q_k) and is driven by pairwise-correlated white noise among all d DAHC pairs at a given frequency. This stochastic forcing approximates the structure of last level's regression residuals, adhering to the stopping criterion for adding layers (Chekroun and Kondrashov, 2017, see Fig. 6). No extra coupling across the frequencies is imposed other than stochastic forcing in Eq. (10) by the same white noise realization. The presented DAHD-SL approach is highly computationally efficient and totally parallelizable. The SL model coefficients can be estimated in parallel for each frequency, the overall number of independent coefficients to estimate remains small and fixed for each DAHC (p_k, q_k)-pair, and the models [Eq. (10)] can be run in parallel across frequencies.

The general functional form of Eq. (10) is rigorously justified by the theory of Ruelle–Pollicott resonances and their estimation by time series of DAHCs (Kondrashov *et al.*, 2018). Note also that the DAHCs associated with $f \equiv 0$ are not paired and resemble red noises in practice, thus only a linear model is used at the zero-frequency; see Kondrashov *et al.* (2015).

Furthermore, any subset of DAHCs can be convolved with its corresponding set of DAHMs, to produce a partial or full reconstruction of the original space-time dataset, respectively. Thus, the following jth *reconstructed component (RC)* at time t and for channel k is defined as

$$R_k^j(t) = \frac{1}{M_t}\sum_{s=L_t}^{U_t} \xi_j(t-s+1)\mathbf{E}_k^j(s), \quad 1 \le s \le M', \tag{11}$$

where L_t (resp. U_t) is a lower (resp. upper) bound in $\{1, \ldots, M'\}$, that is allowed to depend on time. The normalization factor M_t equals M', except near the ends of the time series, and the sum of all the RCs recovers the original time series. The *harmonic reconstruction component (HRC)* is defined using the sum over all indices $j \in \mathcal{J}(f)$ corresponding to a given Fourier frequency f, and it characterizes how associated variability is expressed in the space-time domain,

$$R_k(t;f) = \sum_{j\in\mathcal{J}(f)} R_k^j(t). \tag{12}$$

Fundamentally, DAHD-SL modeling approach is justified by Mori–Zwanzig formalism of statistical mechanics, which has emerged recently as theoretical guidance for stochastic climate modeling (Kondrashov *et al.*, 2015; Palmer, 2019; Ghil and Lucarini, 2020; Lucarini and Chekroun, 2023). It is aimed to construct a prognostic model for evolution of the variables representing targeted spatiotemporal fields—partial observations of the full climate system. The key steps are modeling nonlinear interactions between the targeted variables, and parameterizing as stochastic forcing and memory effects of their cross-interactions with processes not directly included in the model.

The data-driven DAHD-SL approach enables to find such an optimal relationship responsible in sea ice evolution, with memory

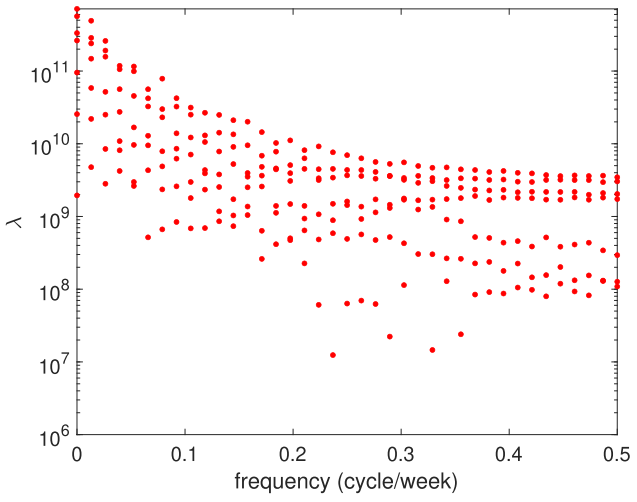

FIG. 5. DAHD spectra for regional Arctic SIE anomalies.

effects conveyed by DAHD time-embedding as well as by nonlinear and stochastic parametrizations in the SL model [Eq. (10)]. The competitive advantage of the DAHD-SL approach is that it reduces the difficult task of modeling complex mixture of temporal scales in original dataset to the simpler situation of a narrow-band time series of DAHCs. These properties of DAHCs, in turn, enable to construct their predictive model within a universal class of coupled frequency-ranked nonlinear stochastic SL oscillators with a few parameters to estimate. Taking a broader view, DAHD-SL resembles spectral methods using operator-theoretic approaches (e.g., transfer or Koopman operators), which aim to identify nearly cyclic observables in a complex nonlinear dynamical system by employing geometric kernel methods combined with delay-embedding methodology (Froyland *et al.*, 2021).

DAHD-SL methodology has shown great promise for a wide variety of challenging geophysical datasets, such as those describing

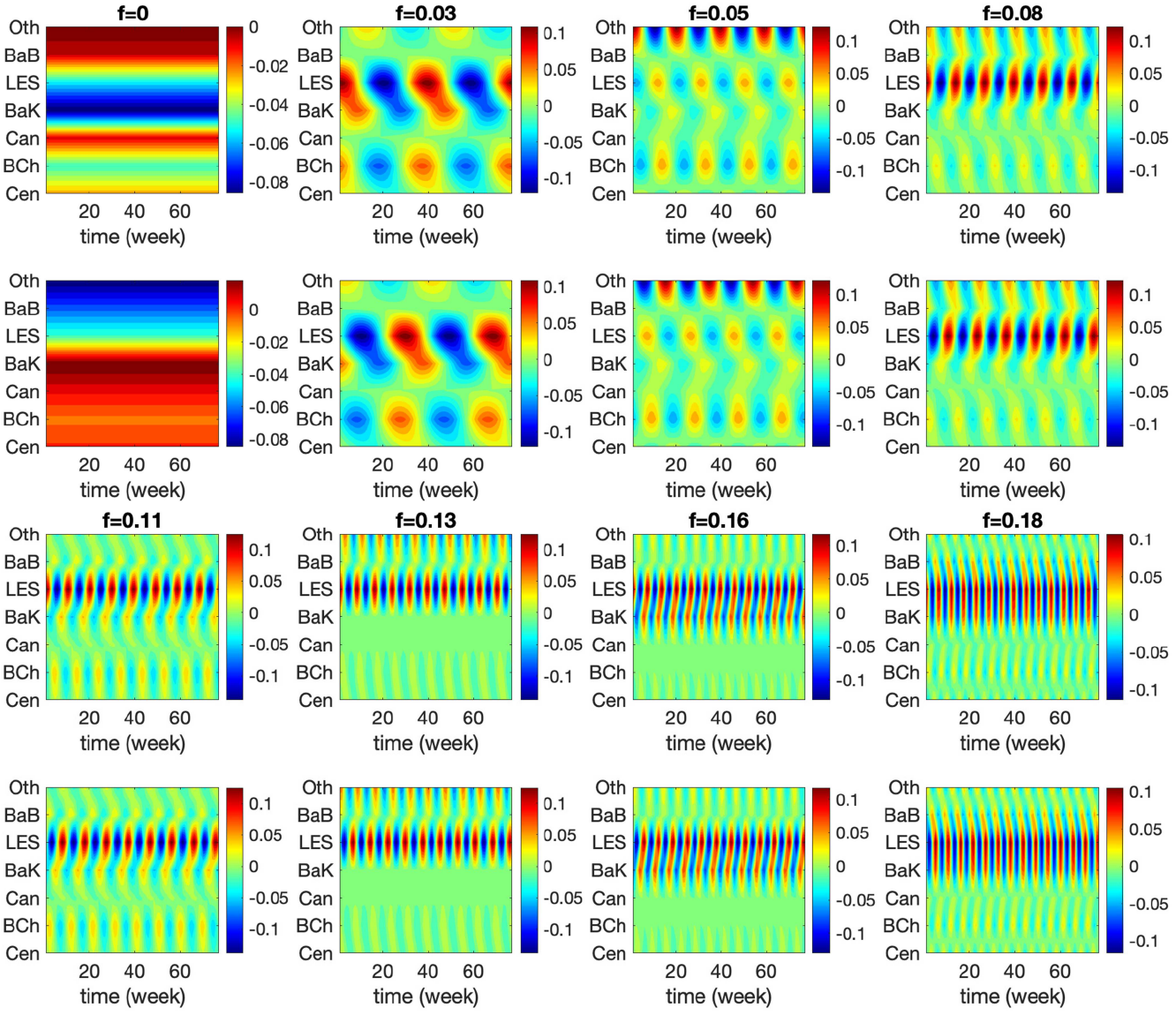

FIG. 6. Space-time patterns of data-adaptive harmonic mode (DAHM) pairs for largest λ at selected frequencies f (cycle/week), see Fig. 5, x-axis—time (weeks), y-axis—Arctic regions: Center (Cen), Beaufort/Chukchi (Bch), Canadian Archipelago (Can), Barents/Kara (BaK), Laptev/East Siberian (LES), Baffin Bay/Greenland Sea (BaB), and Others (Oth), units—non-dimensional. Note that for each $f \neq 0$ the modes in a pair are shifted in time by exactly quarter of associated period $1/f$ [see Eq. (7)], and for $f = 0$ the modes are unpaired.

high-dimensional oceanic turbulent flows (Ryzhov *et al.*, 2019, 2020; Kondrashov *et al.*, 2018, 2020), space physics (Kondrashov and Chekroun, 2017), and for predicting summertime Arctic sea ice extent (Kondrashov *et al.*, 2017, 2018).

IV. PREDICTION

Forecasts are made consistent with existing protocols for submissions into SIO. First, calendar weeks 36–39 that typically align with September are taken to represent the prediction target for SIO. The SL model [Eq. (10)] is trained on data from its beginning in 2006 through the 35th, 31st, 27th, and 23rd calendar week in 2024, when September, August, July, and June predictions are solicited, respectively. In particular, each time when prediction is made, the seasonal cycle and anomalies are recalculated, and DAHD decomposition of the latter is performed by using only data available until the time of the start of the forecast, i.e., it is strictly without look-ahead.

The time-embedding window M is one key parameter in DAHD approach that requires tuning to compute cross-correlation sequence $\rho^{p,q}(m)$ [Eq. (1)]. The optimal M should be large enough to resolve decay of temporal correlations, and at the same time, also not too big in order to obtain robust estimates of model coefficients (Kondrashov *et al.*, 2018). We used $M = 39$ weeks based on prior studies by assessing skill of the retrospective forecasts (Kondrashov *et al.*, 2018). This relatively large time-embedding window of more than nine months also effectively captures memory effects across subseasonal-to-seasonal time scales, contributing to the predictability of summertime Arctic sea ice.

Figure 5 shows typical DAHD power spectrum λ's for regional SIE anomaly time series in seven Arctic regions (Fig. 4), and it is evenly spaced in frequency. The number of frequency bins is determined by the embedding window $M' = 77$ weeks (sampling units), i.e., equal to $(M' + 1)/2 = 39$. There are exactly $d = 7$ DAHD mode pairs (d equals the number of regional input time series) at a given frequency f, except $f = 0$ where there are d single (i.e., unpaired) modes. The DAHD spectrum has more power in intraseasonal band, corresponding to larger anomalies occurring in melt season.

The spatiotemporal patterns of DAHMs shown in Fig. 6 reveal useful dynamical information in the combined evolution and mutual influence of regional SIE anomalies in particular frequency bands. The dominant patterns of the variability, i.e., those corresponding to the pair having largest λ at particular frequency, may convey different co-variability between the regions, such as out-of-phase, in-phase, or time-lagged.

The predictions of DAHCs (see Fig. 7) are obtained by stochastic SL model initialized in 35th, 31st, 27th, and 23rd week and integrated forward $K = 4$, 8, 12, and 16 weeks ahead, for September, August, July, and June solicitations, respectively. The stochastic

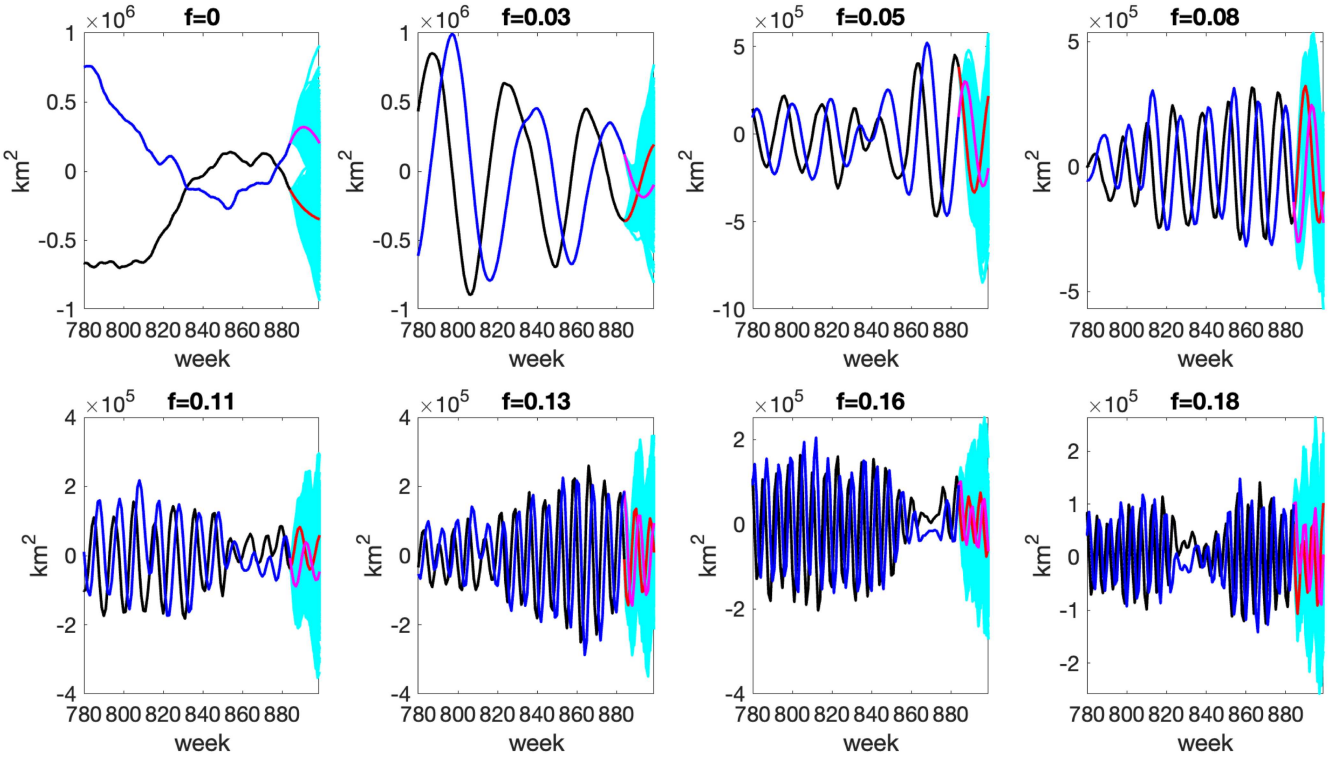

FIG. 7. DAHCs pair (black and blue) time series associated with largest λ at selected frequencies f (cycle/week), consisting of narrowband time series at the same temporal frequency f of the associated DAHMs, but modulated in amplitude; (cyan)—their ensemble predictions by stochastic SL oscillators model initialized in June, and (red and magenta)—ensemble means, respectively; x-axis corresponds to time in weeks, y-axis to SIE in km^2.

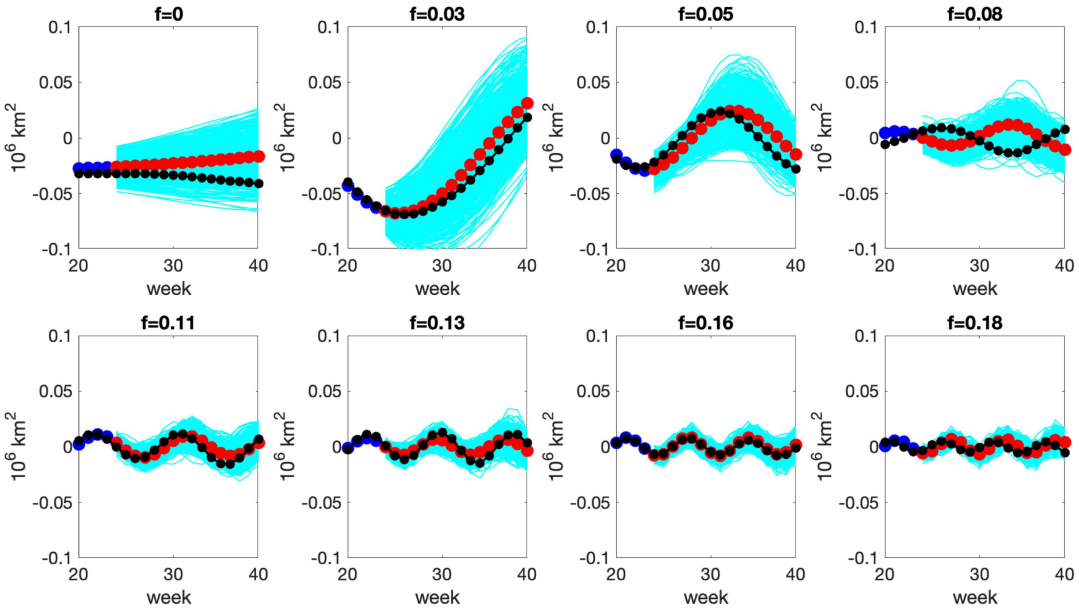

FIG. 8. DAHD June prediction of 2024 summertime SIE anomalies in Beaufort/Chukchi region for HRCs in individual frequency bands. Estimates from observations: (blue)—at prediction time, (black)—at the end of summer; (cyan)—ensemble of DAHD stochastic realizations, and (red)—ensemble mean, frequency f (cycle/week).

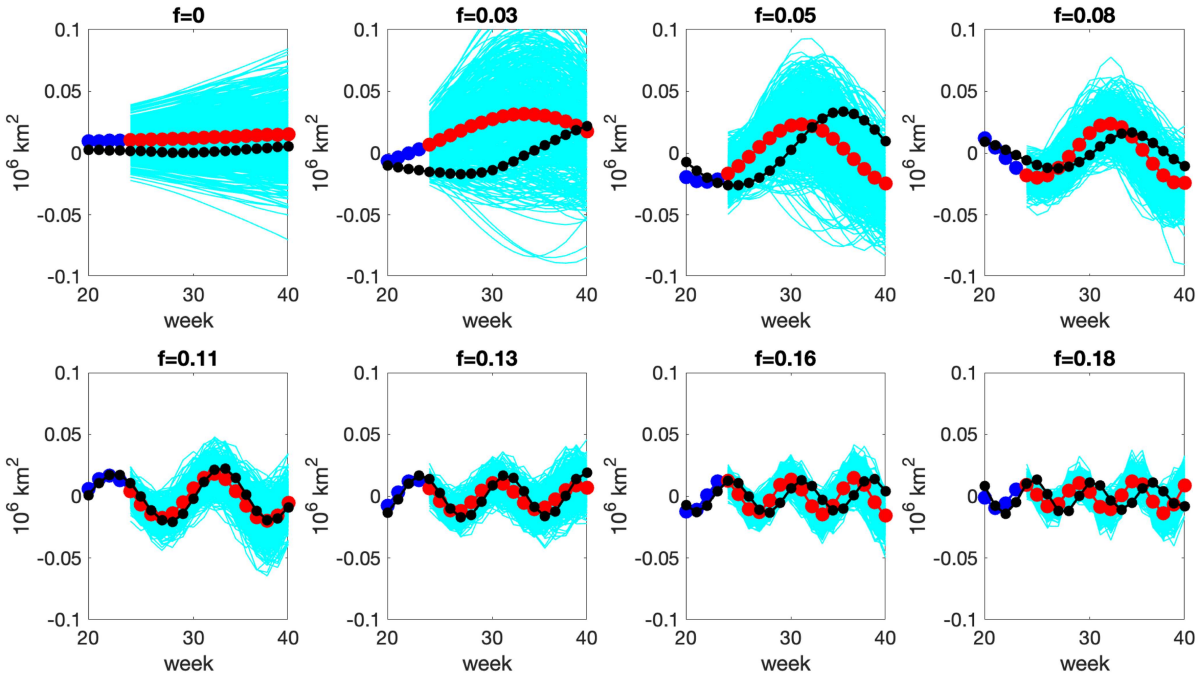

FIG. 9. DAHD June prediction of 2024 summertime SIE anomalies in Laptev/Eastern Siberian region for HRCs in individual frequency bands. Observations: (blue)—at prediction time, (black)—at the end of summer; (cyan)—ensemble of DAHD stochastic realizations, and (red)—ensemble mean, frequency f (cycle/week).

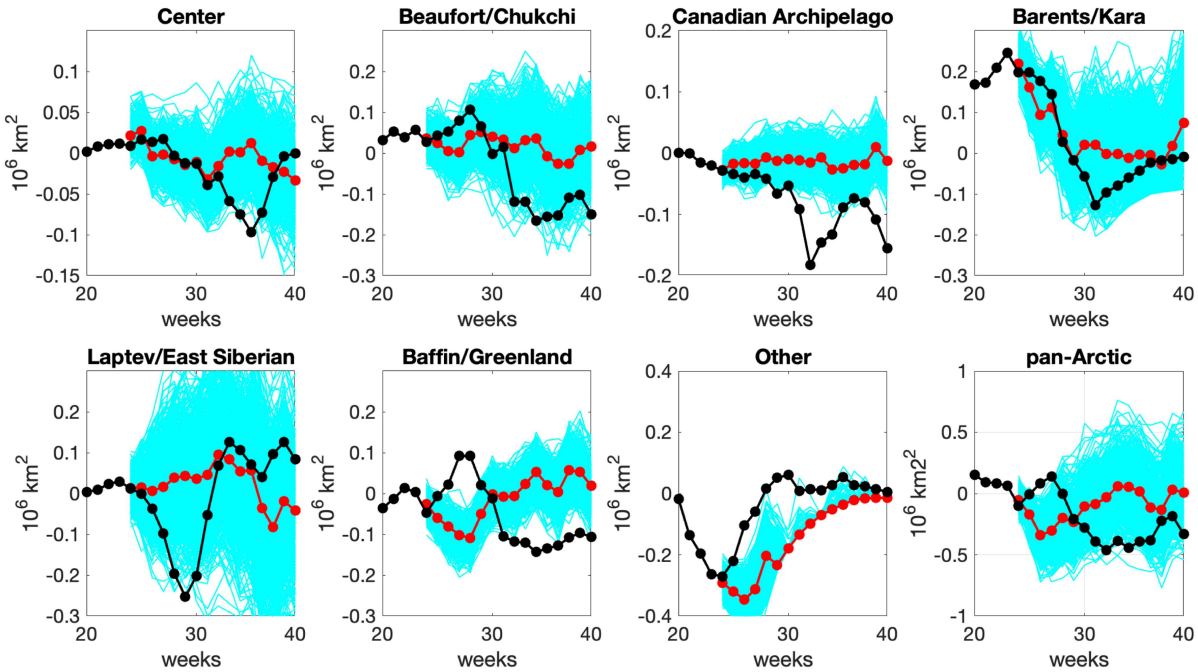

FIG. 10. DAHD prediction of 2024 summertime regional and pan-Arctic SIE anomalies initialized in June: observations (black), (cyan)—ensemble of DAHD stochastic realizations, (red)—ensemble mean.

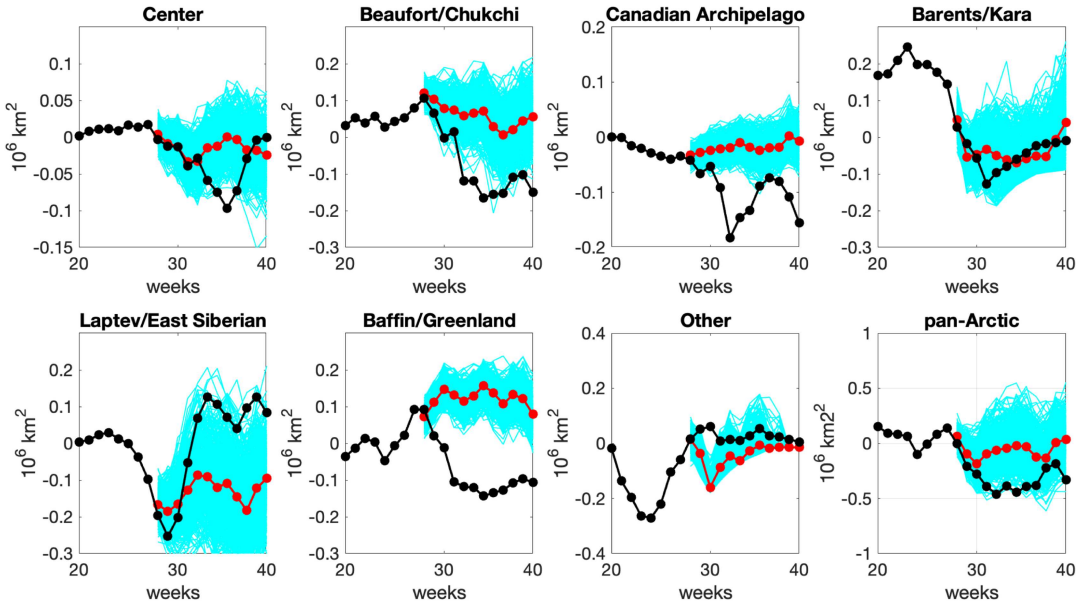

FIG. 11. DAHD prediction of 2024 summertime regional and pan-Arctic SIE anomalies initialized in July: observations (black), (cyan)—ensemble of DAHD realizations, (red)—ensemble mean.

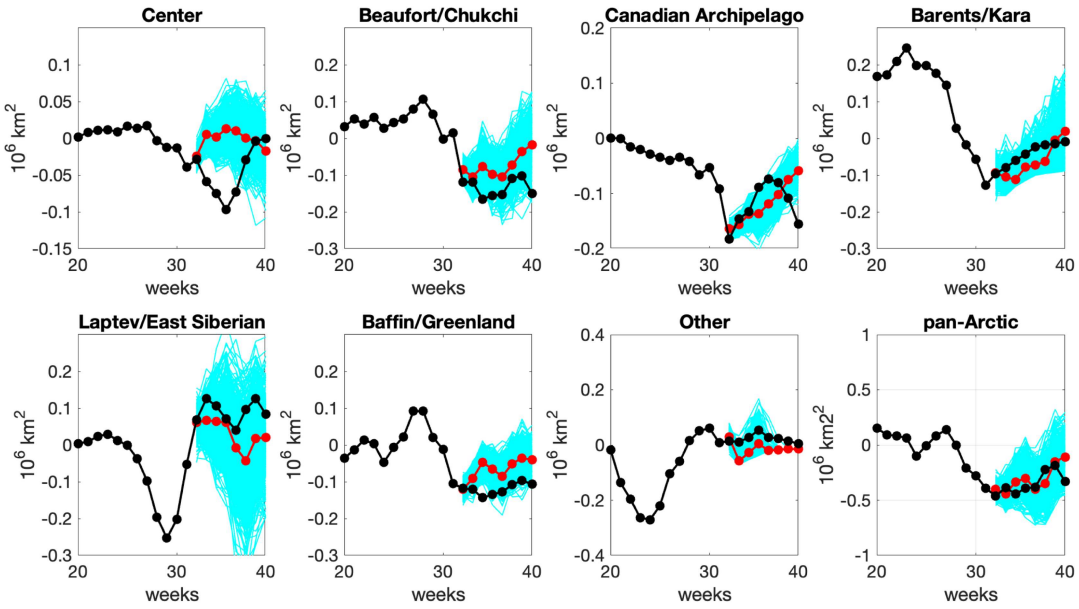

FIG. 12. DAHD prediction of 2024 summertime regional and pan-Arctic SIE anomalies initialized in August: observations (black), (cyan)—ensemble of DAHD stochastic realizations, (red)—ensemble mean.

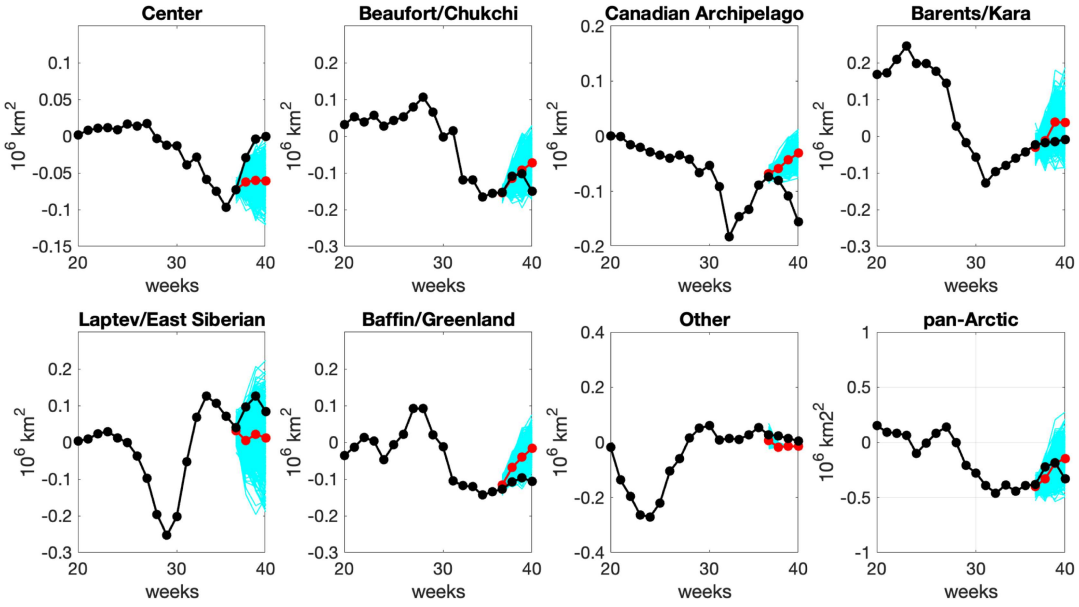

FIG. 13. DAHD prediction of 2024 summertime regional and pan-Arctic SIE anomalies initialized in September: observations (black), (cyan)—ensemble of DAHD stochastic realizations, (red) ensemble mean.

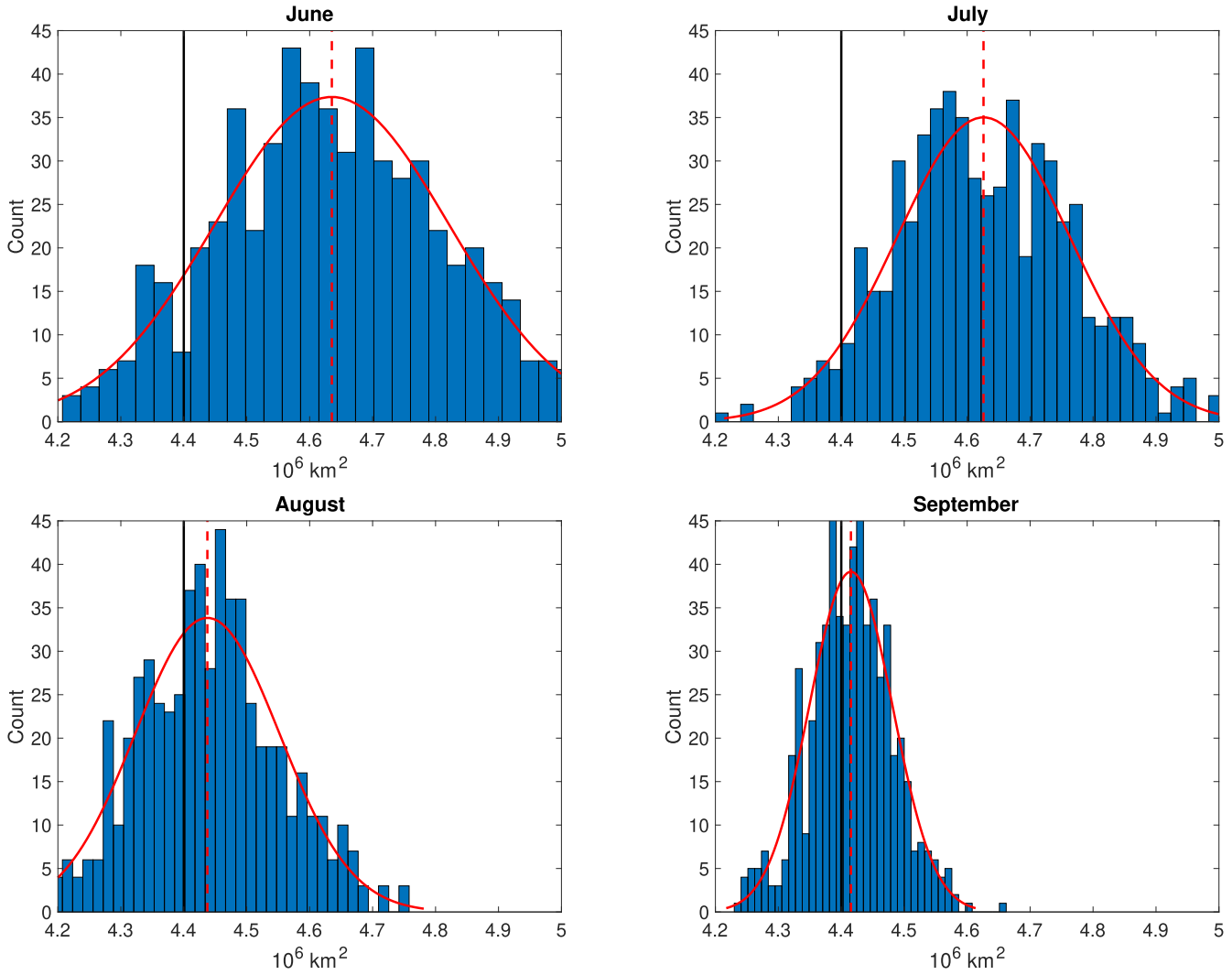

FIG. 14. Histogram of DAHD 600 ensemble member predictions (blue) of Pan-Arctic September 2024 SIE (10^6 km^2) initialized at the beginning of June, July, August and September: (dashed red)—ensemble mean, (solid red)—fitted normal distribution, (solid black)—observed September 2024 SIE of 4.40 10^6 km^2.

model is initialized and then run forward in an ensemble, with each run driven by a particular realization of stochastic forcing. The stochastic ensemble spread at a given lead time provides a natural estimate of the uncertainty for ensemble mean. Predicted DAHCs are combined then with DAHMs to form stochastic ensemble of predictions of HRCs at each predicted frequency. For practical purposes, we use the range $0 \leq f \leq 0.38$ (cycle/week), which captures 99% of the variance in pan-Arctic SIE anomalies [see Eqs. (11) and (12)].

Ensemble members of HRCs corresponding to a particular noise realization are (i) added across the frequencies to yield ensemble predictions of regional SIE anomaly; (ii) the latter is added to the regional seasonal cycle; (iii) the sum over all regions yields total SIE. Note that since SIE cannot be negative, the predicted anomaly may need to be post-processed by adjusting it as needed with respect to seasonal cycle, such as in Barents/Kara and Other regions. We enforce physical non-negativity by truncating predicted SIE at zero as needed before September aggregation; verification metrics are computed on this truncated series. The last four calendar weeks (i.e., 36–39) of predictions are then averaged to obtain September values for SIO submission.

Figures 8 and 9 show June-based predictions of HRCs in different frequency bands for Beaufort/Chukchi and Laptev/East Siberian regions, respectively. For most of frequencies, predictions are fairly consistent and are close to observations. For some frequencies, the prediction may deviate from the observed when estimated at the

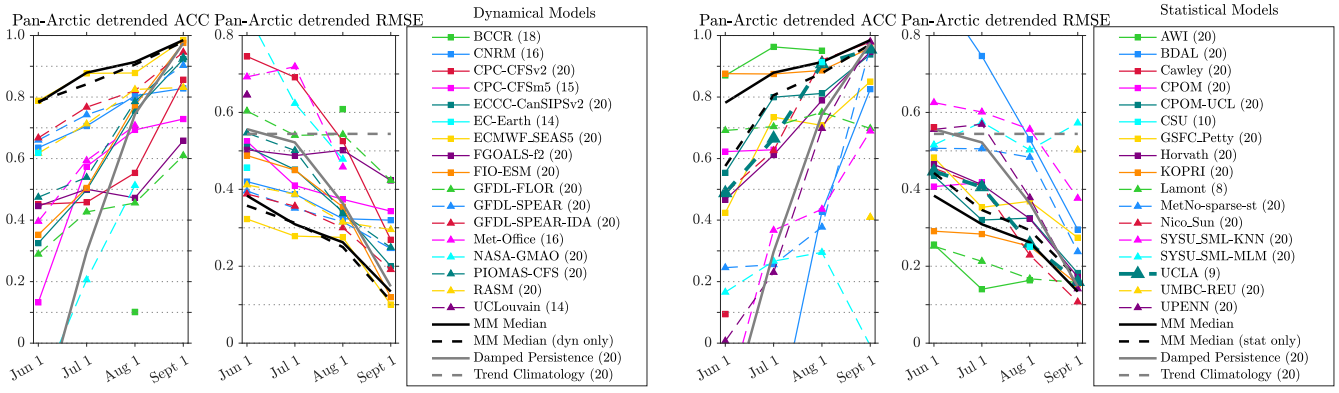

FIG. 15. Multi-model predictive skill for September Pan-Arctic SIE based on Bushuk (2024) dataset from SIO assessment (Bushuk *et al.*, 2024). Skill (RMSE and ACC) is plotted as a function of initialization time (June 1–September 1) and are computed from detrended time series. The numbers in parentheses in the legend indicate the number of years available from each model over the 2001–2020 time period. DAHD-based statistical model is labeled "UCLA.".

end of September. These results can be explained by the complex spatiotemporal structure of SIE anomalies decomposed by DAHD. In particular, highly transient anomalies developing during the melt season when the forecasts are issued may strongly modulate DAHCs of certain spatiotemporal patterns; in turn, it is their reconstructions and predictions, when aggregated spatially in associated frequency bands, may be subject to additional uncertainty. Predictions of less-stable spatiotemporal patterns are effectively averaged out DAHD-SL stochastic ensemble, thus emphasizing more stable and predictable content in the forecasts.

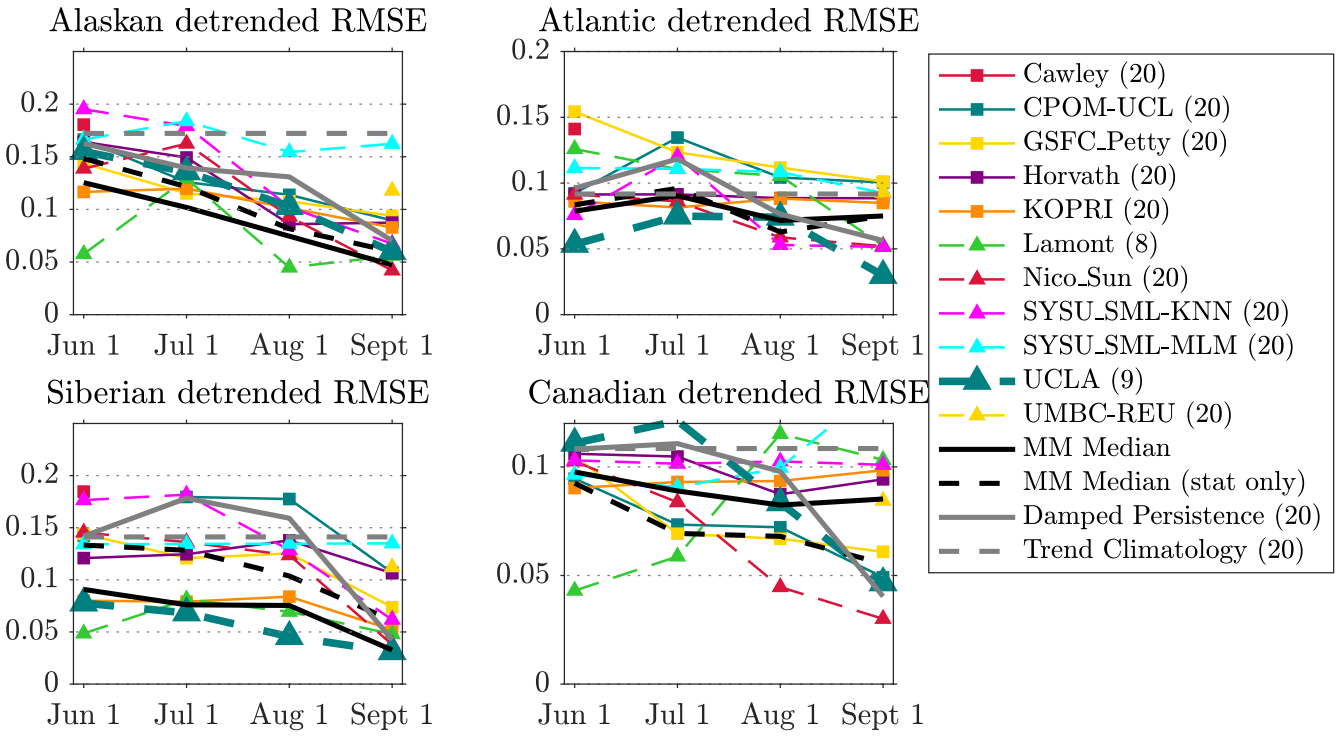

FIG. 16. Similar as in Fig. 15, but RMSE skill for Alaskan, Siberian, Atlantic, and Canadian Seas regions by statistical models only, based on Bushuk (2024) dataset from SIO assessment (Bushuk *et al.*, 2024). DAHD-based model is labeled "UCLA.".

Figures 10–13 show resulting DAHD predictions of 2024 summertime regional and pan-Arctic SIE anomalies when initialized in June, July, August, and September, respectively. While predictions in Barents/Kara region were fairly consistent and accurate throughout the melt season, accuracy of forecasts in other regions—such as Baffin/Greenland, Canadian Archipelago, Beaufort/Chukchi, and Laptev/East Siberian, was affected by large short-term rapid fluctuations that have not been fully captured. Such rapid changes are typically caused by the influence of key ocean-atmosphere variables (air temperature, sea-level pressure, etc., see Sec. II) that are not currently considered in the current DAHD model formulation and thus would be more difficult to predict; inclusion of exogenous ocean-atmosphere information for improving predictions of SIE is left for future research.

Histograms of DAHD stochastic ensemble predictions (Fig. 14) show that the ensemble mean of pan-Arctic September SIE changes modestly between June, July, August, and September outlooks—4.64, 4.63, 4.44, and 4.42 (10^6 km^2), respectively, and with decreasing uncertainty in ensemble spread, as expected, while the observed SIE was 4.40 (10^6 km^2). The real-time DAHD predictions submitted to 2024 SIO were even more accurate: June—4.43 (Bhatt *et al.*, 2024), July—4.42 (Bhatt *et al.*, 2024), August—4.22 (Bhatt *et al.*, 2024), September—4.37 (10^6 km^2) (Bhatt *et al.*, 2024) , but they did not account for above-mentioned post-processing of anomalies to avoid non-physical negative SIE.

V. DISCUSSION

To put above-mentioned DAHD real-time skill for SIO (e.g., RMSE ≈0.3 million km^2, see Sec. I) in perspective, even though a recent assessment of SIO forecasts for 2008–2022 (Blanchard-Wrigglesworth *et al.*, 2023) did not present skill for individual statistical models, as a group, they did outperform dynamical models (see Fig. 1a in Blanchard-Wrigglesworth *et al.*, 2023). Furthermore, the multi-model (both dynamical and statistical) median forecast skill, when initialized in June, is just slightly more skilled (RMSE = 0.48 million km^2) than a damped anomaly forecast, but July and August initialized forecasts (RMSE = 0.52 and 0.36 million km^2, respectively) do not beat this benchmark.

It is also instructive to compare the real-time predictions with retrospective forecasts of regional summertime Arctic sea ice by the DAHD model as part of SIO review paper (Bushuk *et al.*, 2024) on assessment of the multi-model predictive skill was for coupled regions of the Alaskan Seas (Chukchi and Beaufort), Siberian Seas (East Siberian and Laptev), Atlantic Seas (Kara, Barents, and Greenland Seas), and Canadian Seas (Canadian Archipelago and Baffin Bay), and Center region, adding up to Pan-Arctic, and for models initialized June-through-August targeting September. The results of these DAHD-based reforecasts were generally consistent with its real-time SIO predictions over the past 7 years, with good performance except in outlier years of 2012 and 2020 that were " hard to predict" for all SIO-participating models.

The Pan-Arctic RMSE skill of DAHD-based model (labeled as "UCLA") is close to multi-model median of all models (including dynamical) as well as of statistical models only, see Fig. 15, while its regional skill for Atlantic and Siberian Seas is actually best in RMSE among statistical models and dynamical models, see Fig. 16. Very good DAHD skill in Atlantic Seas is notable in particular, because SIE variability occurring in the Greenland, Barents, and Kara Seas is driven by challenging-to-predict anomalies in sea ice export (Kwok, 2008). On the other hand, there is a room for improvement for Canadian and Alaskan Seas.

VI. CONCLUSIONS

In summary, DAHD-based model utilizing SIE data only is already competitive and robust among both physics-based and statistical models in reforecasts and real-time predictions of September Arctic sea ice. The inherent sources of predictability in presented DAHD-SL model stem from a combination of interconnected factors tailored to subseasonal-to-seasonal (S2S) timescales. Temporal autocorrelation, or memory effects, allows recent regional SIE values to influence near-term states, as anomalies in specific Arctic regions can persist over weeks to months due to the dynamics of ice growth, melt, and advection. The pronounced seasonal cycle of freezing and melting within each region provides a predictable baseline, enabling models to forecast S2S transitions, such as the onset of melt or freeze-up in specific sectors. While the long-term decline in SIE due to climate change is less dominant on these shorter timescales, regional trends can still inform predictions, particularly for seasonal forecasts. Also, by leveraging regional data, spatial variability is captured better, detecting localized anomaly patterns, such as regional responses to short-term weather events or ice transport. Low-frequency climate variability, though more relevant to longer timescales, contributes marginally to seasonal predictability by providing a stable background signal. Feedback mechanisms, like the ice-albedo effect, where reduced ice cover in a region increases local heat absorption and accelerates melting, are better resolved with regional data, enhancing the model's ability to predict short-term changes. However, relying solely on regional sea ice extent data limits the incorporation of external drivers, such as atmospheric winds or oceanic heat transport, which are critical for S2S predictability and may constrain forecast accuracy.

DAHD-SL framework allows to test extensively the limits of extended predictability by incorporating additional ice-oceanic-atmospheric data to SIE datasets that may improve presented results further. In a future work, a suite of retrospective forecasts of September Arctic SIE by resulting data-driven multivariate Arctic models initialized prior to June (winter–spring) and through September will allow to assess potential improvements in prediction skill, help to quantify covariability in ice-ocean-atmosphere system and contributing the role of different physical drivers to extended predictability.

ACKNOWLEDGMENTS

This research was supported by National Science Foundation (NSF) under Grant No. OPP-2438993. The collaborative work undertaken at the Tipping Phenomena in Environmental Dynamical Systems workshop was supported by the London Mathematical Society through Grant Scheme 3 (Grant No. 32304). Part of this research was performed while D.K. and I.S. were visiting the

Institute for Mathematical and Statistical Innovation (IMSI), which is supported by the NSF under Grant No. DMS-1929348.

AUTHOR DECLARATIONS

Conflict of Interest

The authors have no conflicts to disclose.

Author Contributions

Dmitri Kondrashov: Conceptualization (equal); Methodology (equal); Software (equal). **Ivan Sudakow:** Funding acquisition (equal); Validation (equal). **Valerie Livina:** Validation (equal); Writing – review & editing (equal). **Qingping Yang:** Visualization (equal); Writing – review & editing (equal).

DATA AVAILABILITY

The data that support the findings of this study are available from the corresponding author upon reasonable request. The NSIDC daily data by region is available at https://nsidc.org/sea-ice-today/sea-ice-tools.

REFERENCES

Bhatt, U., Meier, W., Blanchard-Wrigglesworth, E., Bushuk, M., Stoudt, S., and Taylor, A., see https://www.arcus.org/sipn/sea-ice-outlook/2024/august for "Sea Ice Outlook: 2024 August Report" (2024).

Bhatt, U., Meier, W., Blanchard-Wrigglesworth, E., Bushuk, M., Stoudt, S., and Taylor, A., see https://www.arcus.org/sipn/sea-ice-outlook/2024/july for "Sea Ice Outlook: 2024 July Report" (2024).

Bhatt, U., Meier, W., Blanchard-Wrigglesworth, E., Bushuk, M., Stoudt, S., and Taylor, A., see https://www.arcus.org/sipn/sea-ice-outlook/2024/june for "Sea Ice Outlook: 2024 June Report" (2024).

Bhatt, U., Meier, W., Blanchard-Wrigglesworth, E., Bushuk, M., Stoudt, S., and Taylor, A., see https://www.arcus.org/sipn/sea-ice-outlook/2024/september for "Sea Ice Outlook: 2024 September Report" (2024).

Bhatt, U., Meier, W., Blanchard-Wrigglesworth, E., Massonnet, F., Goessling, H., Ludwig, V., Bieniek, P., Eicken, H., Fisher, M., Hamilton, L. C., Little, J., Overland, J., Serreze, M., Steele, M., Stroeve, J., Walsh, J., Wang, M., and Wiggins, H. V., see https://www.arcus.org/sipn/sea-ice-outlook/2022/post-season for "Sea Ice Outlook: 2022 Post Season Report" (2023).

Bhatt, U. S., Bieniek, P., Bitz, C., Blanchard-Wrigglesworth, E., Eicken, H., Goessling, H., Hamilton, L. C., Hardman, M., Little, J., Massonnet, F., Meier, W., Overland, J. E., Serreze, M., Steele, M., Stroeve, J., Thoman, R., Walsh, J., Wang, M., Wiggins, H. V., and Wood, K., see https://www.arcus.org/sipn/sea-ice-outlook/2019/post-season for "2019 Sea Ice Outlook Full Post-Season Report" (2020).

Bhatt, U. S., Bieniek, P., Bitz, C. M., Blanchard-Wrigglesworth, E., Eicken, H., Fisher, H. M., Goessling, H., Jung, T., Kurths, J., Little, J., Ludwig, V., Massonnet, F., Meier, W., Overland, J. E., Serreze, M., Steele, M., Stroeve, J., Walsh, J., Wang, M., and Wiggins, H. V., see https://www.arcus.org/sipn/sea-ice-outlook/2021/post-season for "2021 Sea Ice Outlook Post-Season Report" (2022).

Bhatt, U. S., Bieniek, P., Blanchard-Wrigglesworth, E., Eicken, H., Goessling, H., Hamilton, L. C., Little, J., Massonnet, F., Meier, W., Overland, J. E., Serreze, M., Steele, M., Stroeve, J., Thoman, R., Wallin, B., Walsh, J., Wang, M., Wayand, N., Wiggins, H. V., and Yuan, X., see https://www.arcus.org/sipn/sea-ice-outlook/2018/post-season for "2018 Sea Ice Outlook Full Post-Season Report" (2019).

Blanchard-Wrigglesworth, E., Bushuk, M., Massonnet, F., Hamilton, L. C., Bitz, C. M., Meier, W. N., and Bhatt, U. S., "Forecast skill of the arctic sea ice outlook 2008–2022," Geophys. Res. Lett. **50**, e2022GL102531, https://doi.org/10.1029/2022GL102531 (2023).

Brunton, S. L., Budišić, M., Kaiser, E., and Kutz, J. N., "Modern Koopman theory for dynamical systems," SIAM Rev. **64**, 229–340 (2022).

Bushuk, M., "Data archive and code for 'Predicting September Arctic Sea Ice: A Multi-Model Seasonal Skill Comparison'," Zenodo (2024). https://doi.org/10.5281/zenodo.12636015.

Bushuk, M., Ali, S., Bailey, D. A., Bao, Q., Batte, L., Bhatt, U. S., Blanchard-Wrigglesworth, E., Blockley, E., Cawley, G., Chi, J., Counillon, F., Coulombe, P. G., Cullather, R. I., Diebold, F. X., Dirkson, A., Exarchou, E., Gobel, M., Gregory, W., Guemas, V., Hamilton, L., He, B., Horvath, S., Ionita, M., Kay, J. E., Kim, E., Kimura, N., Kondrashov, D., Labe, Z. M., Lee, W., Lee, Y. J., Li, C., Li, X., Lin, Y., Liu, Y., Maslowski, W., Massonnet, F., Meier, W. N., Merryfield, W. J., Myint, H., Navarro, J. C. A., Petty, A., Qiao, F., Schroder, D., Schweiger, A., Shu, Q., Sigmond, M., Steele, M., Stroeve, J., Sun, N., Tietsche, S., Tsamados, M., Wang, K., Wang, J., Wang, W., Wang, Y., Wang, Y., Williams, J., Yang, Q., Yuan, X., Zhang, J., and Zhang, Y., "Predicting September arctic sea ice: A multi-model seasonal skill comparison," Bull. Am. Meteorol. Soc. **105**, E1170–E1203 (2024).

Chekroun, M. D. and Kondrashov, D., "Data-adaptive harmonic spectra and multilayer Stuart-Landau models," Chaos **27**, 093110 (2017).

Fetterer, F., Knowles, K., Meier, W., Savoie, M., and Windnagel, A., "Sea ice index, version 3," NASA National Snow and Ice Data Center (2017). doi:10.7265/N5K072F8.

Froyland, G., Giannakis, D., Lintner, B. R., Pike, M., and Slawinska, J., "Spectral analysis of climate dynamics with operator-theoretic approaches," Nat. Commun. **12**, 6570 (2021).

Ghil, M. and Lucarini, V., "The physics of climate variability and climate change," Rev. Mod. Phys. **92**, 035002 (2020).

Hamilton, L. C. and Stroeve, J., "400 predictions: The SEARCH sea ice outlook 2008–2015," Polar Geogr. **39**, 274–287 (2016).

Kondrashov, D. and Chekroun, M. D., "Data-adaptive harmonic analysis and modeling of solar wind-magnetosphere coupling," J. Atmos. Sol.-Terr. Phys. **177**, 179–189 (2018).

Kondrashov, D., Chekroun, M. D., and Berloff, P., "Multiscale Stuart-Landau emulators: Application to wind-driven ocean gyres," Fluids **3**, 21 (2018).

Kondrashov, D., Chekroun, M. D., and Ghil, M., "Data-driven non-Markovian closure models," Physica D **297**, 33–55 (2015).

Kondrashov, D., Chekroun, M. D., and Ghil, M., "Data-adaptive harmonic decomposition and prediction of Arctic sea ice extent," Dyn. Stat. Clim. Syst. **3**, 1–23 (2018).

Kondrashov, D., Chekroun, M. D., Yuan, X., and Ghil, M., "Data-adaptive harmonic decomposition and stochastic modeling of Arctic sea ice," in *Advances in Nonlinear Geosciences*, edited by A. Tsonis (Springer, 2017).

Kondrashov, D., Ryzhov, E. A., and Berloff, P., "Data-adaptive harmonic analysis of oceanic waves and turbulent flows," Chaos **30**, 061105 (2020).

Kwok, R., "Summer sea ice motion from the 18 GHz channel of AMSR-E and the exchange of sea ice between the Pacific and Atlantic sectors," Geophys. Res. Lett. **35**, L03504, https://doi.org/10.1029/2007GL032692 (2008).

Lucarini, V. and Chekroun, M. D., "Theoretical tools for understanding the climate crisis from Hasselmann's programme and beyond," Nat. Rev. Phys. **5**, 744–765 (2023).

Meier, W., Bhatt, U. S., Walsh, J., Thoman, R., Bieniek, P., Bitz, C. M., Blanchard-Wrigglesworth, E., Eicken, H., Hamilton, L. C., Hardman, M., Hunke, E., Jung, T., Kurths, J., Little, J., Massonnet, F., Overland, J. E., Serreze, M., Steele, M., Stroeve, J., Wang, M., and Wiggins, H. V., see https://www.arcus.org/sipn/sea-ice-outlook/2020/post-season for "2020 Sea Ice Outlook Full Post-Season Report" (2021).

Palmer, T. N., "Stochastic weather and climate models," Nat. Phys. **1**, 463–471 (2019).

Percival, D. B. and Walden, A. T., *Spectral Analysis for Physical Applications* (Cambridge University Press, 1993).

Ryzhov, E. A., Kondrashov, D., Agarwal, N., and Berloff, P. S., "On data-driven augmentation of low-resolution ocean model dynamics," Ocean Model. **142**, 101464 (2019).

Ryzhov, E. A., Kondrashov, D., Agarwal, N., McWilliams, J. C., and Berloff, P., "On data-driven induction of the low-frequency variability in a coarse-resolution ocean model," Ocean Model. **153**, 101664 (2020).
Schmidt, O. T., Mengaldo, G., Balsamo, G., and Wedi, N. P., "Spectral empirical orthogonal functions analysis of weather and climate data," Mon. Weather. Rev. **147**, 2979–2995 (2019).
Stern, H. L., "Regime shift in arctic ocean sea-ice extent," Geophys. Res. Lett. **52**, e2024GL114546, https://doi.org/10.1029/2024GL114546 (2025).
Towne, A., Schmidt, O. T., and Colonius, T., "Spectral proper orthogonal decomposition and its relationship to dynamic mode decomposition and resolvent analysis," J. Fluid. Mech. **847**, 821–867 (2018).
Zerenner, T., Goodfellow, M., and Ashwin, P., "Harmonic cross-correlation decomposition for multivariate time series," Phys. Rev. E **103**, 062213 (2021).
Zhen, Y., Chapron, B., Mémin, E., and Peng, L., "Eigenvalues of autocovariance matrix: A practical method to identify the Koopman eigenfrequencies," Phys. Rev. E **105**, 034205 (2022).